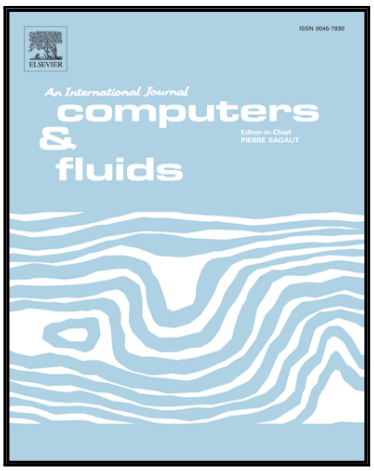

A Level-Set Aided Single-Phase Model for the Numerical Simulation of Free-Surface Flow on Unstructured Meshes

Eugenio Schillaci, Lluís Jofre, Néstor Balcázar, Oriol Lehmkuhl, Assensi Oliva

PII: S0045-7930(16)30281-X
DOI: 10.1016/j.compfluid.2016.09.014
Reference: CAF 3275

To appear in: *Computers and Fluids*

Received date: 16 April 2015
Revised date: 18 April 2016
Accepted date: 12 September 2016

Please cite this article as: Eugenio Schillaci, Lluís Jofre, Néstor Balcázar, Oriol Lehmkuhl, Assensi Oliva, A Level-Set Aided Single-Phase Model for the Numerical Simulation of Free-Surface Flow on Unstructured Meshes, *Computers and Fluids* (2016), doi: 10.1016/j.compfluid.2016.09.014

Highlights

- A new single-phase approach for the numerical simulation of free-surface flows is presented.
- Novel strategy for the deactivation of the light phase built on the level-set function.
- Suitable for rectilinear and unstructured 3-D meshes.
- Increased simulation stability/performance in comparison to two-phase solvers.
- Ease of implementation on previously developed full-domain based codes.

A Level-Set Aided Single-Phase Model for the Numerical Simulation of Free-Surface Flow on Unstructured Meshes

Eugenio Schillaci[a], Lluís Jofre[a], Néstor Balcázar[a], Oriol Lehmkuhl[a,b], Assensi Oliva[a,]

[a] *Heat and Mass Transfer Technological Center (CTTC), Universitat Politècnica de Catalunya - BarcelonaTech, ETSEIAT, Colom 11, 08222 Terrassa (Barcelona), Spain*
[b] *Termo Fluids S.L., Av. Jacquard 97 1-E, 08222 Terrassa (Barcelona), Spain*

Abstract

A new single-phase scheme for the numerical simulation of free-surface problems on 3-D unstructured meshes is presented. The flow field is obtained from the discrete solution of the incompressible Navier-Stokes equations, whereas a conservative level-set method is employed to capture fluid interfaces on an Eulerian approach. The scheme is based on a novel treatment of the interface for the deactivation of the light phase, allowing an optimization of the classic two-phase model for the cases in which the influence of the lighter phase is negligible. The deactivation is performed by directly imposing the appropriate pressure at the surface boundary, and, unlike similar approaches, without the need to treat near-interface velocities. The method is validated against various analytical and experimental references, demonstrating its potential on both hexahedral and unstructured meshes. Moreover, it shows higher

Corresponding author. Tel.: +34 93 739 81 92; Fax: +34 93 739 89 20.
Email address: cttc@cttc.upc.edu (Assensi Oliva)

numerical stability in comparison to two-phase solvers, as well as significant advantages in terms of computational performance.

Keywords: free-surface flow, single-phase scheme, conservative level-set, unstructured 3-D mesh

1. Introduction

A large number of complex engineering applications and physical phenomena require the analysis of the interaction between two or more immiscible phases. Some remarkable examples are the movement of gaseous bubbles inside a liquid phase, the motion and break-up of waves, as well as their interaction with solid boundaries, and the atomization of liquid jets. The issues related to the numerical simulation of these flows are a topic of great interest and lively debate in the scientific community. The main concerns are the resolution of the continuity and Navier-Stokes equations for the conservation of mass and momentum, respectively, and the treatment of the interface between fluids. Several methodologies have been proposed in the past decades to numerically reproduce the movement of interfaces, involving many diverse strategies; a general overview is presented by Scardovelli and Zaleski [1]. However, they can be distributed into two main groups di□ering in the way in which the detection of the interface is globally conceived and each of which appears to be particularly suitable for the simulation of specific cases.

The first group collects the approaches in which the interface between

fluids is tracked as it moves (interface-tracking methods). For instance, in the Arbitrary Lagrangian Eulerian (ALE) technique [2], the tracking is done by means of a moving (Lagrangian) grid that follows the interface, while the fluid evolves on a fixed stationary (Eulerian) mesh. Another example is the Front Tracking (FT) method [3], in which the individual interfaces are represented by sets of connected marker points. Generally, these methodologies are not e□cient in the simulation of complex vortical flows, in which significant distortions of the interface topology may occur [4].

The strategies corresponding to the second main group (interface-capturing methods) are characterized by a scalar function, $\phi(\mathbf{x}, t)$, that embeds the moving interface on a fixed grid. This function, which identifies the interfacial regions according to di□erent criteria, is usually advected by means of a transport equation, written in the case of divergence-free velocity fields as

$$\frac{\partial \phi(\mathbf{x}, t)}{\partial t} + \quad \cdot (\phi(\mathbf{x}, t)\mathbf{u}) = 0. \tag{1}$$

These latter methods are adaptable to a larger range of configurations, as they can handle intrinsically any topological change of the interface, including breakage and reconnection. Nevertheless, their implementation requires more e□ort in the treatment of the interface and in the identification of the geometric properties, such as normal vectors and curvatures. Two main interface-capturing strategies are the Volume-of-Fluid (VOF) and Level-Set (LS).

In VOF methods [5], the advected function is the volume fraction scalar field, $\phi(\mathbf{x}, t)$, of one of the phases. Its value is 1 or 0 in the cells totally filled by that phase or totally empty, while it varies from 0 to 1 in the interface zone, where the cells are partially filled by the two phases. Due to the discontinuity of the color function, a method must be found to avoid the diffusion of the interface when advected, as it must remain sharp. The main option is to reconstruct the interface before the advection step, for instance, using a Piecewise Linear Interface Calculation (PLIC) scheme, on which many of the advanced modern algorithms are based. This method consists in reconstructing geometrically the line, or the plane in a 3-D case, that delimits the interface in the cells where both phases are present, ensuring that the volume of the different phases is preserved. One of the simplest schemes was proposed by Youngs [6], and is based on evaluating the interface normal as the normalized gradient of $\phi(\mathbf{x}, t)$. Up to now, the VOF/PLIC method has been extended to a wide variety of configurations, including 2-D and 3-D implementations both on Cartesian and unstructured meshes, and reaching in all cases first- and second-order accuracy [7, 8, 9, 10]. However, despite ensuring mass conservation, the accurate evaluation of interface properties, such as curvature, is complex due to the discontinuous nature of the volume fraction scalar field advected by the VOF method [11]. Moreover, due to its geometrical basis, the process of evaluating these properties can be rather time consuming if a reasonable accuracy is expected [17].

Alternatively, in the LS method [12] the interface is identified by the zero

contour of a signed level-set function, advected at every time step. Once reached the new position, the function must be re-initialized to remain a signed distance, positive on one side of the interface, and negative on the other. The level-set function is continuous, hence, the values of viscosity and density of the two phases in contact vary smoothly across the interface, giving numerical robustness to the algorithm. The Standard Level-Set method (SLS) is characterized by simplicity of implementation, and by the possibility to extract interface parameters without supplementary e□orts. Moreover, it is adaptable to a wide range of situations maintaining a high order of accuracy, as demonstrated by Osher and Sethian [12] and by Sussman et al. [13]. Nevertheless, a big drawback of the method is the fact that it is not mass conservative, as the volume bounded by the zero contour is not preserved exactly when advected and re-initialized. This has been recently tackled by Olsson and Kreiss [14, 15] by means of introducing the Conservative Level-Set (CLS) method. Their approach advects the level-set function, while at the same time ensures mass conservation, by using Total Variation Diminishing (TVD) strategies and specially treating the level-set re-initialization process. Therefore, CLS methods improve mass conservation, however, at expenses of encumbering the evaluation of interface properties. Other authors have followed this approach to achieve accurate results on 3-D unstructured [16, 17] and curvilinear [18] meshes, using di□erent types of mass conservation schemes [19], and extending it to turbulent atomization [20] and compressible flows [21].

The aforementioned interface-capturing strategies are usually coupled to the discrete solution of the Navier-Stokes equations to provide a numerical framework for the simulation of all the phases involved in a multi-phase flow. In this work, we will refer to this scheme as full-domain model. However, in some engineering applications involving the interaction of two fluids, usually a liquid and a gas, the classic two-phase simulation can be simplified by limiting the calculations to the single liquid phase. This occurs when the interface between the two phases behaves as a free-surface, i.e. it is subjected to constant perpendicular normal stress and it is free from parallel shear solicitations. In such cases, the pressure at the free-surface can be approximated to the free-stream value, e.g. atmospheric pressure. This simplification applies only to the cases in which the gaseous phase has no e□ect on the physics of the problem. Hence, it should not be expected the formation of gaseous bubbles, nor the presence of stresses in the liquid phase generated by the gas, due for example to its pressurization in a section of the domain. These assumptions are usually fulfilled in ocean engineering problems, such as the simulation of wave motion and its interaction with submerged or semi-submerged obstacles. The adoption of this strategy, to which we will refer to as single-phase model, can lead to consistent savings in computational time as a result of the deactivation of the light phase. Moreover, the transition from a full-domain model to a single-phase one simplifies the problem, resulting in more stable numerical schemes due to the disappearance of high density ratios along the interface. In the deactivation

process, the additional resources spent for the individuation of the transition region, as well as for the enforcement of pressure and velocity conditions at the interface, are counterbalanced by the computational memory saved to update numerical operators in the light phase. Therefore, as demonstrated in this work, the single-phase scheme reduces significantly the time-to-solution and memory requirements with respect to the full-domain approach, while not appreciably a□ecting the physics of the problem.

In the past years, researchers have developed various types of single-phase models, mainly di□ering in the way in which the process of deactivating the light phase is carried out. To mention some, in Löhner et al. [22], VOF and LS techniques are used to advect the interface, and the scalar fields are de-activated for the light phase. Then, in order to ensure the correct advection of the volume fractions, pressure and velocity are evaluated at the interface by extrapolation from the values of the points inside the liquid region. Lv et al. [23] employed a similar scheme for the pressure-velocity extension, but the interface capturing was accomplished by means of a hybrid LS/VOF strategy. Kleefsman et al. [24] utilized a VOF method and interpolated both pressure and velocities at the interface. Carrica et al. [25] and Di Mascio et al. [26] used Standard Level-Set approaches, imposed the pressure value at the free-surface to enforce the jump conditions by directly intervening on the pressure equation, and extended the velocity field in order to correctly transport the level-set function. Finally, Enright et al. [27] applied hybrid particle/Level-Set methodologies to impose internal pressure boundary con-

ditions, and extrapolated velocity across the interface.

In this work, we propose a novel strategy to solve the liquid phase on an Eulerian grid by explicitly imposing the pressure at the free-surface and deactivating the light phase. The interface is transported by means of the CLS method proposed by Olsson and Kreiss [14] and extended to 3-D unstructured meshes in Balcázar et al. [16]. This CLS method, further verified and validated in [28, 29], allows robust numerical simulations even on coarse grids. At the same time, it facilitates the deactivation process, as the same level-set function provides a convenient tool to identify the interface. The resolution of the Navier-Stokes equations on the interfacial region avoids the requirement to extrapolate the velocity field. Consequently, the costly process of evaluating interpolation stencils at every iteration is spared, thus, making the algorithm easier to implement and resulting in faster computations. In order to check the convergence of the numerical method, the verification process begins with the analysis of the spurious currents on the interface of a static liquid column. Next, the method is tested on a series of problems in which the assumptions of free-surface and the physical independence from the light phase —no bubble formation, no gas pressurization— are fulfilled. These correspond to the sloshing of a linear wave inside a fixed basin, the viscous damping of a solitary wave in shallow water, and the dam-breaking problem; first for the classic 2-D case, and second, in a more complex 3-D configuration. The results are compared to the ones obtained by means of the full-domain model and to the available experimental data, focusing on

the discrepancy between the results and the savings in computational time.

This article is organized as follows. In Sec. 2, the governing equations for the conservation of mass, momentum and volume fraction are presented. The advantages of the single-phase approach in comparison to the full-model are comprehensively discussed in Sec. 3, as well as the numerical discretization and the light phase deactivation process. In Sec. 4 the results obtained from the simulations, and their comparison to the benchmark solutions are discussed. Finally, conclusions are given in Sec. 5.

2. Governing equations

The CLS method is employed to capture the free moving interface in an incompressible and transient two-phase flow. In detail, this work uses the CLS scheme implemented and verified in [16], in which the level-set function, $\phi(\mathbf{x}, t)$, is a regularized distance function defined as

$$\phi(\mathbf{x}, t) = \frac{1}{2}\left(\tanh\left(\frac{d(\mathbf{x}, t)}{2\varepsilon}\right) + 1\right), \tag{2}$$

with $d(\mathbf{x}, t)$ the signed distance function from the interface and ε a parameter that controls the interface thickness. The interface is defined as the set of points for which the regularized function equals 0.5, namely

$$\Gamma = \{x | \phi(\mathbf{x}, t) = 0.5\}. \tag{3}$$

The interface movement is described by the advection equation, where the velocity field $\mathbf{u}$ is provided by the discrete solution of the Navier-Stokes equations. In a divergence-free velocity field, it takes the form reported in Eq. (1). In order to maintain a constant interface width, the CLS function is re-initialized at every time step. This is enforced by the expression

$$\frac{\partial \phi(\mathbf{x},t)}{\partial \tau} + \quad \cdot \phi(\mathbf{x},t)(1-\phi(\mathbf{x},t))\mathbf{n}_{\tau=0} = \quad \cdot \varepsilon \quad \phi(\mathbf{x},t), \tag{4}$$

where τ is the re-initialization pseudo-time, $\cdot \varepsilon \quad \phi$ is the artificial diffusion term —added to avoid discontinuities and to keep the interface thickness constant— and $\cdot \phi(1-\phi)\mathbf{n}_{\tau=0}$ is the compressive flux term, which acts as an interface sharpener at every time step. The unit vector normal to the interface, $\mathbf{n}$, and the interface curvature, $\kappa(\phi)$, are obtained from the level-set function as

$$\mathbf{n} = \frac{\phi}{\phi}, \tag{5}$$

$$\kappa(\phi) = - \quad \cdot \mathbf{n}. \tag{6}$$

On the other hand, multi-phase flows are globally governed by the continuity and Navier-Stokes (NS) equations, which in a domain occupied by two incompressible fluids —labeled below as $i = 1, 2$— separated by an interface Γ, correspond to

$$\cdot \mathbf{u} = 0, \tag{7}$$

$$\frac{\partial(\rho \mathbf{u})}{\partial t} + \quad \cdot (\rho \mathbf{u}\mathbf{u}) = - \quad p + \quad \cdot (\mu[\quad \mathbf{u} + (\quad \mathbf{u})^T]) + \mathbf{S}, \tag{8}$$

where $\mathbf{u}$ is the velocity vector, p is the pressure, ρ is the density, μ is the dynamic viscosity, and $\mathbf{S}$ includes the volumetric sources, given by

$$\mathbf{S} = \rho\mathbf{g} + \sigma\kappa\mathbf{n}\delta_\Gamma, \tag{9}$$

being $\rho\mathbf{g}$ the gravity contribution, and $\sigma\kappa\mathbf{n}\delta_\Gamma$ the surface tension between the fluids, localized at the interface by means of the Dirac delta function δ_Γ. This force constitutes the unbalance between the stresses of the two phases at the interface, and it is evaluated considering the surface tension coe□cient, σ, constant —condition applicable for isothermal flow. It is worth stressing that the incompressibility constraint, $\cdot\,\mathbf{u} = 0$, applies at the interface if assuming the same velocity for the two phases, i.e. no-slip jump conditions.

The discrete solution of the NS equations provides the evolution of the velocity field at every point in the domain, with the transport properties ρ and μ evaluated from the updated $\phi(\mathbf{x}, t)$ values as

$$\rho = \rho_1\phi(\mathbf{x}, t) + \rho_2(1 - \phi(\mathbf{x}, t)), \tag{10}$$

$$\mu = \mu_1\phi(\mathbf{x}, t) + \mu_2(1 - \phi(\mathbf{x}, t)). \tag{11}$$

This yields a transition region —where $\phi(\mathbf{x}, t)$ varies from 0 to 1—, in which the properties vary smoothly. The thickness of this region is controlled by the parameter ε. Thus, by choosing a small ε, a thin interface that sharply defines the separation between the two phases is obtained. However, in order

to avoid numerical instabilities caused by the sudden jump of pressure, ε cannot be too small in comparison to the characteristic mesh length [16].

3. Numerical model

The continuity and Navier-Stokes equations, Eqs. (7) and (8), are discretized over an unstructured grid according to the finite-volume, staggered scheme proposed by Perot [30] and analyzed on 3-D meshes by Jofre et al. [31]. The discrete solution is obtained by applying a fractional step projection method together with an explicit time integration. The staggered scheme stores the scalar quantities at cell centers, while the velocity —considered through the mass flux— is evaluated directly at cell faces. Finally, cell centered velocities are obtained from the interpolation of face values. This scheme ensures the discrete conservation of mass, momentum and kinetic energy. Moreover, the staggered numerical scheme is generally more stable for multi-phase flows than the collocated one [31], to which it has been preferred —further proof of the higher stability is given in Sec. 4.1.

In the following subsections, the discretization of the fluid motion and level-set equations for the full-domain solver on 3-D unstructured meshes is described. In addition, the advantages brought by the use of a single-phase method are discussed, together with the modifications required to obtain the single-phase approximation.

3.1. Full-domain discretization

In this section, subscripts c and f refer, respectively, to cell and face values, nb refers to the neighbor cells that share a face with c, A_f is the face surface, V_c is the cell volume, and $\mathbf{n}_f$ is the face normal vector. Subscripts a and b refer to the cells that lie on the two sides of face f, and W_a and W_b are the distances between face and cell circumcenters, with $W_f = W_a + W_b$ the distance between two neighboring cell circumcenters —see Fig. (1). Since a staggered scheme is used, the velocity is stored at cell faces through the face normal mass flux, and the two quantities are related according to the relation

$$M_f = \rho_f A_f \mathbf{u}_f \cdot \mathbf{n}_f. \tag{12}$$

The time step, Δt, needed to integrate the equations of fluid motion and interface advection, is evaluated according to an e□cient self-adaptive strategy proposed by Trias and Lehmkuhl [32], in which the linear stability domain of the time-integration method is dynamically adapted in order to maximize the time step value.

3.1.1. Equations of fluid motion

Continuity and Navier-Stokes equations are numerically solved by means of the fractional step projection method [33]. The direct dependence between velocity and pressure is uncoupled through the introduction of the predicted

velocity concept, $\mathbf{u}^p$, expressed as

$$\mathbf{u}^p = \mathbf{u}^{n+1} + \frac{\Delta t}{\rho^{n+1}} \quad p^{n+1}. \tag{13}$$

The equation for the evolution of the normal face velocity is obtained by discretizing Eq. (8) over the face CV (highlighted in Fig. (1)), and later, applying the scalar product with $\mathbf{n}_f$ —although high-order time advancement schemes are utilized in the simulations, a first-order description is presented to simplify the exposition—, resulting in the following expression

$$W_f A_f \rho_f^{n+1} \frac{\mathbf{u}_f^{n+1} - \mathbf{u}_f^n}{\Delta t} \cdot \mathbf{n}_f + (W_a \mathbf{c}_a^n + W_b \mathbf{c}_b^n) A_f \cdot \mathbf{n}_f =$$
$$- (p_b^{n+1} - p_a^{n+1}) A_f + (W_a \mathbf{d}_a^n + W_b \mathbf{d}_b^n) A_f \cdot \mathbf{n}_f + (W_a \mathbf{s}_a^n + W_b \mathbf{s}_b^n) A_f \cdot \mathbf{n}_f, \tag{14}$$

where $\mathbf{c}$, $\mathbf{d}$ and $\mathbf{s}$ are the non-volumetric cell-centered discretizations of the convective, diusive and source terms of the neighboring cells, whose contributions are weighted by factors W_a and W_b. Similarly, the correction of the velocity field to enforce mass conservation, Eq. (13), is discretized over face CV as

$$\rho_f^{n+1} A_f \mathbf{u}_f^p \cdot \mathbf{n}_f = \rho_f^{n+1} A_f \mathbf{u}_f^{n+1} \cdot \mathbf{n}_f + \Delta t (p_b^{n+1} - p_a^{n+1}) \frac{A_f}{W_f}. \tag{15}$$

Next, introducing the mass flux definition as in Eq. (12), and rearranging

terms, the last two equations are rewritten as

$$W_f \frac{M_f^{n+1} - M_f^n}{\Delta t} = -(p_b^{n+1} - p_a^{n+1}) A_f - [W_a(\mathbf{c}_a^n - \mathbf{d}_a^n - \mathbf{s}_a^{n+1}) + W_b(\mathbf{c}_b^n - \mathbf{d}_b^n - \mathbf{s}_b^{n+1})] A_f \cdot \mathbf{n}_f, \tag{16}$$

$$M_f^{n+1} = M_f^p - \Delta t(p_b^{n+1} - p_a^{n+1}) \frac{A_f}{W_f}, \tag{17}$$

Finally, Eq. (17) is introduced into Eq. (16) in order to obtain an explicit expression for the evaluation of the predictor face normal mass flux, M_f^p, of the form

$$M_f^p = M_f^n - \Delta t[W_a(\mathbf{c}_a^n - \mathbf{d}_a^n - \mathbf{s}_a^{n+1}) + W_b(\mathbf{c}_b^n - \mathbf{d}_b^n - \mathbf{s}_b^{n+1})] \cdot \mathbf{n}_f \frac{A_f}{W_f}. \tag{18}$$

The convective and diffusive contributions are obtained by integrating the corresponding terms over the cell CV (depicted in Fig. (1)), applying the divergence theorem and discretizing over the cell faces, thus, yielding the expressions

$$\mathbf{c}_c^n = \frac{1}{V_c} \sum_{f \; F(c)} \psi_f^n \hat{M}_f^n, \quad \mathbf{d}_c^n = \frac{1}{V_c} \sum_{f \; F(c)} \mu_f^n \left[(\mathbf{u}_{nb}^n - \mathbf{u}_c^n) \frac{A_f}{d_f} + \quad ^T \mathbf{u}_f^n \cdot \hat{\mathbf{n}}_f A_f \right], \tag{19}$$

where ψ_f is the convected face velocity, $\hat{M}_f$ is the outward face normal mass flux, $\hat{\mathbf{n}}_f$ is the outward face normal vector, d_f is the distance between the nodes of the cells adjacent to face f, and $F(c)$ is the group of faces belonging to cell c.

The discrete pressure field is obtained from Eq. (13). This is accomplished by first applying to it the divergence operator, and later introducing the incompressibility constraint, Eq. (7), such that the dependency in $\mathbf{u}^{n+1}$ is removed from the equation

$$\cdot \mathbf{u}^{p} = \quad \cdot \left(\frac{\Delta t}{\rho^{n+1}} \quad p^{n+1} \right). \tag{20}$$

Next, the equation is integrated over the cell CV, and the divergence theorem is applied, resulting in

$$\int_{\partial V_c} \mathbf{u}^{p} \cdot \mathbf{n}_f d\mathbf{S} = \Delta t \int_{\partial V_c} \frac{p^{n+1}}{\rho^{n+1}} \cdot \mathbf{n}_f dS. \tag{21}$$

Finally, discretizing over cell faces and introducing the mass flux definition, Eq. 12, the following Poisson linear system is obtained

$$\sum_{f \quad F(c)} \frac{\hat{M}_f^{p}}{\rho_f^{n+1}} = \Delta t \sum_{f \quad F(c)} (p_{nb}^{n+1} - p_c^{n+1}) \frac{A_f}{W_f \rho_f^{n+1}}, \tag{22}$$

where the unknown is the pressure field p^{n+1}. In its final form, this linear system is rearranged by introducing the cell coe□cient a_c, the neighbor coe□cients a_{nb}, and the source term b as

$$p_c^{n+1} a_c = \sum_{f \quad F(c)} p_{nb}^{n+1} a_{nb} + b, \tag{23}$$

$$a_c = \sum_{f \ F(c)} a_{nb}, \quad a_{nb} = \Delta t \frac{A_f}{W_f \rho_f^{n+1}}, \quad b = - \sum_{f \ F(c)} \frac{\hat{M}_f^p}{\rho_f^{n+1}}, \tag{24}$$

and it is solved by means of an iterative Preconditioned Conjugate Gradient (PCG) solver [34].

As previously indicated, the staggered scheme requires an interpolation for the evaluation of cell center velocities. This is done by extending the scheme proposed in [30] to the variable-density case. In this way, considering an uniform momentum field ($\rho \mathbf{u}$) over the cell volume, the cell centered velocity is evaluated as the weighted average of the surrounding face mass fluxes, expressed as

$$\mathbf{u}_c^{n+1} = \frac{1}{\rho_c V_c} \sum_{f \ F(c)} \hat{M}_f^{n+1} \mathbf{r}_f^c, \tag{25}$$

where $\mathbf{r}_f^c$ is the weight of the components, as it expresses the distance between cell circumcenter and face centroids.

Finally, considerations regarding the convection scheme chosen to evaluate convected face velocities, ψ_f, are discussed. The upwind (UP) scheme presents good stability properties, since it adds artificial numerical dissipation into the discrete system [35]. In this case, the convective contribution, Eq. (19), is evaluated as follows

$$\mathbf{c}_c^n = \frac{1}{V_c} \sum_{f \ F(c)} \psi_f^n \hat{M}_f^n = \frac{1}{V_c} \sum_{f \ F(c)} \max(\hat{M}_f^n, 0) \psi_{f,c}^n - \max(-\hat{M}_f^n, 0) \psi_{f,nb}^n. \tag{26}$$

However, in cases where turbulence plays a major role, for example, in breaking waves, artificial dissipation is not a desired characteristic for a convection

scheme. Instead, the symmetry-preserving scheme, proposed by Verstappen and Veldman [37] for turbulent flows, is chosen to compute the convected face velocities as

$$\psi_f = \frac{1}{2}(\mathbf{u}_{nb} + \mathbf{u}_c), \tag{27}$$

since it has been demonstrated by Fuster [38] to properly preserve kinetic energy also in multi-phase flows. This practice avoids the error in the conservation of kinetic energy, but may instabilize the solution close to the interface when dealing with not sufficiently fine meshes. Therefore, both UP and SP schemes are adopted in this work, depending on the characteristics of the particular problem.

3.1.2. Level-set equation

The normalized level-set function, $\phi(\mathbf{x}, t)$, is numerically advected after every time step by the $\mathbf{u}^{n+1}$ velocity field, and re-initialized to maintain the interface sharp. At the beginning of the simulation, $\phi(\mathbf{x}, 0)$ is evaluated from the signed distance function to the interface of the initial configuration, $d(\mathbf{x}, 0)$, according to Eq. (2).

In the following steps, the advection of $\phi(\mathbf{x}, t)$ is carried out by integrating Eq. (1) over the cell CV, and applying the divergence theorem to the second term as

$$\int_{V_c} \frac{\partial \phi(\mathbf{x}, t)}{\partial t} dV + \int_{\partial V_c} \phi(\mathbf{x}, t)\mathbf{u} \cdot \mathbf{n}_f dS = 0. \tag{28}$$

The equation is advanced in time according to an explicit scheme. A first-order scheme is used here for simplicity, while a third order Runge-Kutta

(RK3) scheme is employed in the numerical simulations of Sec. 4. Discretizing the convective term over cell faces, the equation reads

$$\frac{\phi_c^{n+1} - \phi_c^n}{\Delta t} V_c + \sum_{f \ F(c)} \hat{U}_f^n A_f \phi_f^n = 0, \tag{29}$$

where $\hat{U}_f^n A_f = \hat{M}_f^n / \rho_f$ is the outward face velocity per unit area, calculated from the outward face normal mass flux, and ϕ_f^n is the advected value of the level set function. In order to enhance solution accuracy and stability, ϕ_f^n is evaluated according to a flux limiter scheme. In particular, the Total Variation Diminishing (TVD) scheme proposed by Sweby [39] and adapted to 3-D unstructured meshes by Balcázar et al. [16] is used, in which the convective operator is evaluated as the sum of an upwind and an anti-diffusive term, expressed as

$$\begin{aligned} \sum_{f \ F(c)} \hat{U}_f^n A_f \phi_f^n = & \sum_{f \ F(c)} \max(\hat{U}_f^n A_f, 0) \phi_{f,c}^n - \max(-\hat{U}_f^n A_f, 0) \phi_{f,nb}^n \\ & + \frac{1}{2} \hat{U}_f^n A_f f_L(\phi) (\phi_{f,nb}^n - \phi_{f,c}^n), \end{aligned} \tag{30}$$

being $f_L(\phi)$ a Superbee limiter function.

Similarly, the re-initialization equation, Eq. (4), is integrated over the cell CV, and the divergence theorem is applied to the convective and diffusive

terms

$$\int_{V_c} \frac{\partial \phi(\mathbf{x},t)}{\partial \tau} dV + \int_{\partial V_c} \phi(\mathbf{x},t)(1-\phi(\mathbf{x},t)\mathbf{n}_{\tau=0} \cdot \mathbf{n}_f dS = \int_{\partial V_c} \varepsilon \quad \phi(\mathbf{x},t) \cdot \mathbf{n}_f dS. \tag{31}$$

Next, the equation is rewritten by advancing the solution in pseudo-time according to an explicit first-order scheme —a TVD-RK3 [40] scheme is used in simulations—, and discretizing compressive and diusive terms over cell faces as

$$\frac{\phi_c^{n+1} - \phi_c^n}{\Delta\tau} V_c + \sum_{f \quad F(c)} \phi_f^n(1-\phi_f^n)\mathbf{n}_{\tau=0} \cdot \mathbf{n}_f A_f = \sum_{f \quad F(c)} \varepsilon_f \quad \phi_f \cdot \mathbf{n}_f A_f, \tag{32}$$

where face value terms are evaluated by means of a central dierence (CD) scheme.

The re-initialization process depends on two numerical parameters, C_ε and C_τ, whose values are determined from preliminary tests. The ε parameter, which controls the thickness of the interface, is evaluated as

$$\varepsilon = C_\varepsilon \Delta h_c, \tag{33}$$

with Δh_c as the characteristic cell size, and $C_\varepsilon = 0.5$. The pseudo-time step, $\Delta\tau$, is evaluated according to a CFL-like criteria, dominated by the diusive contribution, which is given by

$$\Delta\tau = C_\tau \min\left(\frac{\Delta h_c^2}{\varepsilon}\right). \tag{34}$$

The solution requires few iterations in pseudo-time (typically between 3 and 4) for convergence of the level-set function when setting C_τ = 0.01.

3.1.3. Solution algorithm

In summary, the complete algorithm for the resolution of the equations of fluid motion and advancement/re-initialization of the level-set function consists in the following steps:

- Calculate the predicted face normal mass flux, M_f^p, from Eq. (18).
- Update the pressure field, p^{n+1}, by iteratively solving Eq. (23).
- Evaluate the new face mass flux, M_f^{n+1}, as given by Eq. (17).
- Interpolate cell centered velocities, $\mathbf{u}_c^{n+1}$, as proposed in Eq. (25).
- Advect and re-initialize $\phi(\mathbf{x}, t)$ according to Eqs. (29) and (32).

3.2. Single-phase discretization

As introduced in Sec. 1, when the solution of the light phase does not affect the global behavior of the flow, and its analysis can be considered not essential for the scope of the simulation, it may be convenient to specialize the full-domain solver in order to improve its performance. For this purpose, the adoption of a single-phase model is presented.

In this model, the interface is still advected, but it is treated as a moving internal boundary with the scalar and vector fields of the light density phase deactivated. This method can lead to several advantages. For instance,

in multi-phase flows with high density ratios —as in the air-water case—, spurious currents may appear at the interface. They are due to the improper propagation of pressure gradients from the high-density phase to the low-density one, excessively accelerating it and, consequently, making it lose its divergence [23]. Conversely, single-phase solvers usually show more stable behaviors, due to the light-phase deactivation, and consequent reduction of density jumps. Additionally, the consideration of just one phase facilitates the iterative solution of the Poisson linear system, Eq. (23), leading to a reduction in computational costs.

Another advantage is related to the evaluation of the time step. In air-water flows, the time step is mainly limited by the maximum velocity of the air, which can be orders of magnitude larger than the velocity of the water. This is usually consequence of spurious currents advected from the water phase, or excessive acceleration due to geometrical or physical features of the problem configuration. Consequently, deactivating the light phase leads to an overall decrease of the maximum velocity, and to a consequent increase of the time step.

The deactivation is carried out modifying the Poisson linear system, Eq. (23), and the face normal mass flux expression, Eq. (17), i.e. steps 2 and 3 of the solution algorithm proposed in Sec. 3.1.3. The level-set function, $\phi(\mathbf{x}, t)$, is used as a tool to identify the interface region, since it directly indicates the volume fraction of one of the phases —in this work, the heavy phase one. The process starts by choosing a value of ϕ between 0 and 1 (e.g.

ϕ_{lim} = 0.5) that identifies the limit at which the solution of the two-phase flow has to be cut. Hence, as shown in the example of Fig. (2), the cells located in the interface region are individuated and tagged as state cells (SC) according to the following scheme:

- SC1: cells in heavy phase located just below the interface. They are identified as the cells with $\phi > \phi_{\text{lim}}$, presenting at least one neighbor cell with $\phi <= \phi_{\text{lim}}$.
- SC2: after completely defining SC1 cells, SC2 cells correspond to the ones with $\phi <= \phi_{\text{lim}}$ and at least a SC1 neighbor cell.

The Poisson linear system, is modified according to the jump condition proposed by Kang et al. [41], written as

$$[p] - 2[\mu](\quad \mathbf{u} \cdot \mathbf{n}) \cdot \mathbf{n} = \sigma\kappa, \tag{35}$$

where the [·] notation defines the jump of that quantity across the interface. In the case of smeared out viscosity —guaranteed by the smooth distribution of properties at the interface—, the pressure di□erence reduces to $[p] = \sigma\kappa$. Further setting the air pressure to the atmospheric value, p_{atm}, results in the following expression for free-surface pressure

$$p_{fs} = p_{\text{atm}} + \sigma\kappa. \tag{36}$$

Thus, the imposition of a given pressure at the free-surface is achieved mod-

ifying the coe□cients of Eq. (23) for the SC2 cells; the neighbor coe□cients, a_{nb}, are set to 0, the central coe□cient, a_c, is changed to 1, while the source term, b, is modified such that it is equal to the free-surface pressure value. In the same way, the pressure is set to p_{atm} everywhere in the light phase. The strategy is summarized as

$$
\begin{aligned}
a_c &= \begin{cases} \sum_{f \;\; F(c)} a_{nb} & \text{if} \quad \phi > \phi_{\text{lim}}, \\ 1 & \text{if} \quad \phi <= \phi_{\text{lim}}, \end{cases} \\
a_{nb} &= \begin{cases} \Delta t \frac{A_f}{W_f \rho_f^{n+1}} & \text{if} \quad \phi > \phi_{\text{lim}}, \\ 0 & \text{if} \quad \phi <= \phi_{\text{lim}}, \end{cases} \\
b &= \begin{cases} - \sum_{f \;\; F(c)} \frac{\hat{M}_f^p}{\rho_f^{n+1}} & \text{if} \quad \phi > \phi_{\text{lim}}, \\ p_{\text{atm}} + \sigma\kappa & \text{if} \quad \phi = \phi_{\text{lim}} \text{ (SC2 cells)}, \\ p_{\text{atm}} & \text{if} \quad \phi < \phi_{\text{lim}}. \end{cases}
\end{aligned}
\tag{37}
$$

Furthermore, assuming the surface tension negligible for the class of problems considered —mainly marine applications—, the free-surface pressure can be directly set to p_{atm}.

The next step is to consider all the cell pairs, a and b, that lie on the two sides of a face f. Then, the face normal mass flux is evaluated according to Eq. (17) in the heavy phase, whereas it is deactivated in the light one, as

described below

$$M_f^{n+1} = \begin{cases} 0 & \text{if } \phi(a) <= \phi_{\text{lim}} \text{ and } \phi(b) <= \phi_{\text{lim}} \\ M_f^p - \Delta t(p_b^{n+1} - p_a^{n+1})\frac{A_f}{(W_a+W_b)} & \text{otherwise} \end{cases}. \tag{38}$$

Thus, cell center velocities assume non-zero values only for the heavy phase.

3.2.1. Interface advection

In terms of the level-set advection and re-initialization equations, Eqs. 1 and 4, no particular intervention is required. However, the volume fraction value of the heavy phase that identifies the deactivation limit, ϕ_{lim}, plays an important role in the correct advection of the fluid interface. As explained in Sec. 2, the level-set function is used to evaluate the transport properties on the entire domain, even in the interfacial region. Therefore, recalling that $\phi(\mathbf{x}, t) = 1$ in the heavy phase region, and evaluating Eq. (10) for $\phi(\mathbf{x}, t) = 1$ and ϕ_{lim}, the higher and lower possible density values are obtained, which respectively correspond to $\rho_{max} = \rho_1$ and $\rho_{min} = \rho_2 + \phi_{\text{lim}}(\rho_1 - \rho_2)$. Consequently, the larger attainable density difference at the interface is

$$\Delta\rho = \rho_{max} - \rho_{min} = (1 - \phi_{\text{lim}})(\rho_1 - \rho_2). \tag{39}$$

Therefore, as the ϕ_{lim} value gets closer to 1, the range of densities involved in the numerical solution is reduced. This overall reduction leads to a minimiza-

tion of the spurious currents, resulting in faster and more stable numerical calculations. On the other hand, as grid points on the interface zone are deactivated, part of the heavy phase inertia is also neglected. Consequently, a correct velocity field extrapolation is needed to ensure a proper interface advection. The accuracy of the extrapolation becomes increasingly important as the value ϕ_{lim} tends to 1, since it is necessary to extract, and approximate, more and more information of the interface movement from the heavy phase [22, 23]. Nevertheless, from previous work [42], this extrapolation is only effective if the velocity presents a stable and predictable profile, as for example, in the case of progressive waves. In other more complex scenarios, such as the collapse of water columns, this approach is not accurate due to the strong variations in the velocity profile.

On the contrary, as the value ϕ_{lim} is shifted towards 0, a smaller amount of inertia is neglected. It has been found that above a certain lower limit, which depends on the particular case, a velocity field extrapolation does not lead to any change in the solution of the heavy phase flow. Indeed, all the information necessary for its proper advection is obtained from the flow motion algorithm. This procedure avoids the extrapolation of the velocity field across the interface, thus, limiting the error on the final solution that can be caused by any erroneous or not accurate velocity extension.

Generally, the adoption of $\phi_{\text{lim}} \leq 0.01$ makes the method effective for all the cases analyzed. However, the numerical tests reported in this work are carried out by choosing the highest possible ϕ_{lim} value such that veloc-

ity extrapolations are not required to obtain a correct solution. This helps to maximize the benefits obtained from the single-phase approach in terms of stability and velocity. In the next Section, the adopted value of ϕ_{lim} is specified case by case.

4. Numerical tests

This section presents numerical results corresponding to the verification and validation of the proposed single-phase scheme. First, the appearance of spurious currents for the full-domain and single-phase approaches is analyzed for a static liquid column in Sec. 4.1. A first comparison between numerical results and analytical data is performed in Sec. 4.2 by solving the wave sloshing problem. The possibility of integrating the single-phase strategy with a wave maker is assessed in Sec. 4.3. Finally, the well-established dam break problem is numerically simulated, first for a 2-D configuration, Sec. 4.4, and later for a more complex 3-D geometry, Sec. 4.5. In both cases, the numerical results are compared to experimental data.

4.1. Static liquid column

Large density differences between fluids may result in interfacial spurious currents. This first test analyzes the appearance of such currents and their intensity in the case of utilizing the full-domain (2-P) or the single-phase (1-P) approach. For 1-P cases, the deactivation limit, ϕ_{lim}, is set to 0.1. The UP scheme is used for the discretization of the convective operator in the Navier-Stokes equations. The set-up consists of a unit square of side L, occupied

in its lower half by the liquid phase, and subjected to the action of gravity with negligible surface tension. No-slip boundary conditions are imposed on the walls. Given the static nature of this case, the rise of any velocity at the interface corresponds to a non-physical solution. The intensity of the spurious currents is measured by means of the Froude number, Fr, evaluated as

$$\mathrm{Fr} = \frac{|\mathbf{u}|}{\mathbf{g}L}, \tag{40}$$

where $|\mathbf{u}|$ is the average velocity norm of the fluid at the interface. Since the analytical solution of the problem is a zero velocity field, the Froude number at steady state constitutes itself the norm of the error.

In a first test, performed on a Cartesian coarse mesh with 1.6×10^3 cells, the same density value is assigned to the two fluids. For this case, the spurious currents intensity turn out to be negligible (of the order of 10^{-16}) for both 1-P and 2-P solvers. As a second test, a large density difference is imposed between the two phases ($\Delta\rho$ = 1000), therefore, a larger magnitude of spurious currents is expected. In order to evaluate the accuracy of the method, a mesh convergence analysis is performed on progressively finer Cartesian meshes. The results presented in Fig. (3) for the Staggered (Stagg.) discretization show that the error is larger for the 2-P scheme. This demonstrates the effectiveness of the 1-P method in reducing spurious velocities due to the decrease of the density differences, as explained in Sec. 3.2.

In order to compare the staggered and collocated (Coll.) mesh schemes,

the same tests are performed using the Coll. discretization described in [31] and adapted to the multi-phase case. Results show that the Stagg. formulation maintains a lower Fr than Coll. both for 1-P and 2-P models, thus, confirming its higher stability. On the other side, the Coll. scheme demonstrates to be more accurate, as the order of accuracy, p, measured in the proposed series of tests is higher. A summary of the orders of accuracy of the analyzed methods is reported in Tab. 1.

Mesh	Model	p
Stagg.	1-P	1.45
Stagg.	2-P	1.55
Coll.	1-P	1.68
Coll.	2-P	1.8

Table 1: Order of accuracy of the single-phase (1-P) and full-domain (2-P) models used in this work, in combination with both staggered (Stagg.) and collocated (Coll.) mesh schemes. p is evaluated from a mesh convergence analysis performed on the static liquid column case.

4.2. Wave sloshing

The first validation test consists in the analysis of the oscillating movement of a viscous liquid within a stationary 2-D rectangular vessel closed on all its sides. At time t = 0, the wave elevation over the calm liquid column, h_l, is described by the following sinusoidal function

$$\eta(x, 0) = \eta_0 \cos\left[\kappa(x + \frac{\lambda}{2})\right], \tag{41}$$

where $\kappa = 2\pi/\lambda$ is the wave period, λ is the wavelength and η_0 is the wave amplitude. The results obtained from the analysis of the temporal evolution of the wave height are compared to the analytical function proposed by Wu et al. [43]. If assuming sufficiently high Reynolds number and supposing a negligible influence of the finite depth of the tank, the wave evolution in time and space is described by the following expression

$$\frac{\eta_{ref}(x,t)}{\eta(x,0)} = 1 - \frac{1}{1 + 4\nu_l^2 \frac{\kappa^2}{g}} \left[1 - e^{-2\nu_l \kappa^2 t} \left(\cos \sqrt{\kappa g} t + 2\nu_l \kappa^2 \frac{\sin \sqrt{\kappa g} t}{\sqrt{\kappa g}} \right) \right], \quad (42)$$

where $\nu_l = \mu_l/\rho_l$ is the kinematic viscosity of the liquid and g is the norm of the gravity acceleration. The analytical solution allows the validation of the model for different values of density and viscosity of the liquid phase. These features are taken into account by means of the Reynolds number, that in free-surface problems can be defined as

$$Re = \frac{h_l \sqrt{h_l g}}{\nu_l}. \quad (43)$$

In the simulations, λ is set to 1 in order to obtain a wave with period $\kappa = 2\pi$, while the rectangular vessel is $w = 2\lambda$ in width. The initial wave amplitude, η_0, is 0.02 m, and the calm liquid depth is set to 1 m. The simulations are performed on a Cartesian mesh with 1.7×10^5 cells, distributed more densely in the zone of the interface. No-slip boundary conditions are applied to all the non-periodic boundaries of the domain. From preliminary observations,

the deactivation limit ϕ_{lim} value is set to 0.1 —valid for all the cases involving the undulating movement of a liquid reservoir. A pure SP convection scheme is used for the discretization of ψ_f in Eq. (19), since the high density of cells in the interface region reduces the amount of spurious currents.

In the first test (High Re), fluid density and viscosity are set to the values of water at room temperature —ρ_l = 998 kg/m^3, μ_l = 1.003 × 10^{-3} Pa · s. The resulting Reynolds number is Re 1 × 10^6. In Fig. (4(a)), the time evolution of the relative wave height at the center of the domain, x_c, is shown. Time is indicated in dimensionless form as t = $t\sqrt{g/h_l}$. Due to the predominance of inertia forces, the wave oscillates almost undisturbed for a large number of time periods. As shown in the figure, the numerical solution, $\eta(x_c, t)/\eta_0$, agrees with the analytical data, $\eta_{ref}(x_c, t)/\eta_0$. In the next case (Low Re), density and viscosity of the liquid are chosen such that Re 1 × 10^3. The plot in Fig. (4(b)) shows a marked reduction of the wave height as the simulation is advanced in time, since viscous forces dominate the physics. In this scenario, the numerical results obtained from the 1-P scheme also agree with analytical data.

4.3. Solitary wave

In the following problem, the capability of the single-phase approach to correctly reproduce the viscous damping of water in intermediate or low depth basins is analyzed. Moreover, this test examines the potential of the single-phase scheme in incorporating a wave maker into the simulation. A

wave maker consists in analytically forcing the solution of the level-set function and/or the scalar fields on a small part of the domain, such that a specific free-surface profile is numerically obtained. In order to ensure numerical stability in the wave maker zone, the forcing (analytical) function, $\xi_{for}(\mathbf{x},t)$, is coupled to the numerical solution, $\xi_{num}(\mathbf{x},t)$, by means of a relaxation parameter, $\psi(x,t)$, written as

$$\xi(\mathbf{x},t) = \xi_{for}(\mathbf{x},t)(1-\psi(x,t)) + \xi_{num}(\mathbf{x},t), \tag{44}$$

where $\psi(x,t)$ varies smoothly in the $x-$axis from 0 at $x = 0$ to 1 at the end of the wave maker zone. The free-surface flow simulated in this test corresponds to a solitary wave traveling from the left to the right part of the domain. It consists in an aperiodic and non-linear displacement of water above the calm water level that can be produced mechanically by an instantaneous impulse. As proposed by Mei [44], the analytical solution of the wave profile takes the form

$$\eta(x,t) = a\cosh^{-1/2}\sqrt{\frac{3a}{4h_w^3}}(x - C\,t), \tag{45}$$

with a as the wave amplitude, h_w as the calm water depth, and C as the wave speed defined as

$$C = \sqrt{g(h_w + a)}. \tag{46}$$

The motion of a solitary wave is usually characterized by its wave crest advancement and height. The latter caused by the viscous forces and, as

given by [44], described by the following expression

$$H(t)^{-1/4} = a^{-1/4} + 0.08356\sqrt{\frac{\nu_w}{(gh_w)^{1/2}h_w^{3/2}}}\frac{C\ t}{h_w}. \tag{47}$$

The simulation is carried out with Re 1 × 10^3, as given by Eq. (43), such that the viscous e□ects increase the amount of wave damping. The computational domain consists in a long, narrow tank (32 m long and 2 m high) initially filled in its lower part by water at rest. The domain is discretized in 4.5 × 10^5 cells stretched, according to a hyperbolic distribution, at the zone in which the passage of the wave crest is expected. No-slip boundary conditions are imposed at the tank bottom, while Neumann conditions apply on the left, right and top boundaries of the domain. In this test, the UP convection scheme is used to minimize the presence of spurious currents. On the right part of the domain, viscosity is artificially increased in order to provide extra amount of damping before the wave reaches the boundary. Similar to the previous case, ϕ_{lim} is set to 0.1.

The wave —h_w = 1.0 m, a = 0.15 m— is generated on the left part of the domain, as depicted in Fig. (5(a)), where it progressively enters the pure numerical zone. Once fully generated, Fig. (5(b)), the wave continues its path through the domain with an almost constant velocity, Figs. (5(c)) and (5(d)), preserving its form, but slowly reducing its height.

The evolution in time[1] of the wave height, $Y = H(t) + h_w$, and advance-

[1]On the plots, the initial time is set equal to the value at which the wave exits the wave

ment on the $x-$axis, X, are shown in Fig. (6), as well as its comparison to the analytical solution.

A small number of time steps are required to stabilize the solution when the wave enters the pure numerical zone. Consequently, a slightly difference between the analytical and the numerical solution is noticeable at the initial stage of the simulation, both in Figs. (6(a)) and (6(b)). However, once stabilized, the numerical solution closely follows the analytical values of wave height and advancement.

In conclusion, this test is a good demonstration that a wave maker can be coupled to the single-phase scheme. The wave configuration can be easily adapted to model progressive waves, in linear or composed form, which are representative of ocean waves and their interaction with fixed or floating obstacles. For instance, in [42] the single-phase approach is used to simulate the interaction between progressive waves and an oscillating water column system for the extraction of energy from sea waves.

4.4. Dam break 2-D

The problem of the dam break consists in simulating the collapse of a water column, initially at rest, under the action of gravity. It is one of the most widely used benchmark for the validation of free-surface models, due to its easy set-up, the simplicity of the boundary conditions required, and the presence of several references in the literature, both experimental and

maker zone, t_0.

numerical. The initial configuration is depicted in Fig. (7), where the physical properties of the fluids are also reported, mimicking water and air conditions at room temperature. The initial water column presents rectangular shape with side length a = 4.5 in, and the proportion f between rectangle height and length is 1. No-slip boundary conditions are imposed at the solid walls of the container, Neumann conditions apply at the top in order to mimic an open boundary, whereas periodic conditions are set on the front and back boundaries.

The numerical results obtained are compared to the experimental data reported in Martin and Moyce [45], in which several experiments were performed on the fall of a water column, considering various options for the initial column shape and proportions. In the experimental set-up of the reference, vacuum conditions were established, thus, making licit the numerical single-phase approximation. Moreover, the independence of the flow from the periodic boundaries is assessed, which allows the 2-D approximation.

The results are presented in dimensionless form. In particular, the magnitudes studied are the dimensionless residual height, H , of the water column and the dimensionless leading front, Z , of the wave generated by the water collapse, given by

$$H = \frac{H}{a \cdot f}, \quad t_H = t\sqrt{\frac{g}{a}}, \quad Z = \frac{Z}{a}, \quad t_Z = t\sqrt{\frac{g \cdot f}{a}}, \tag{48}$$

where H is the measured residual height, Z is the measured leading edge,

Test	Model	Mesh	No. cells
1	2-P	STR	3.7×10^4
2	1-P	STR	3.7×10^4
3	1-P	UNSTR	5.0×10^4

Table 2: List of the numerical experiments performed for the 2-D dam break case.

and t_H and t_Z are the corresponding dimensionless time indicators.

In order to highlight differences due to the air phase deactivation, the simulations are performed by means of the 1-P and 2-P approaches. A pure UP scheme is used for the discretization of the convective term in the momentum equations, such that spurious velocities are efficiently damped. The different simulations performed are listed in Tab. 2, where STR corresponds to a Cartesian mesh with 3.7×10^4 control volumes ($\Delta h \quad 1.46 \times 10^{-3}$), while UNSTR refers to an unstructured mesh with 5×10^4 triangular elements ($\Delta h \quad 2 \times 10^{-3}$). In order to accurately capture the advancement of the wave front, the deactivation limit is set to 0.01.

The comparison between numerical results and experimental data is shown in Fig. (8), up to the instant in which the wave front reaches the right boundary of the domain. According to the STR mesh results (tests 1 and 2), the numerical simulations faithfully follow the experimental values for H . On the other hand, numerical Z values are initially higher than the experimental ones. This trend has been reported in similar studies [16, 46], and its explanation is probably related to the influence of the mechanical apparatus that releases the water column in the early stages of the experiment. Despite this

initial difference, the numerical results agree with the experimental data. In terms of differences between the 1-P and 2-P simulations, it is noticed that: (1) the H values practically overlap; (2) the speed of propagation is very similar, and the wave fronts reach the opposite wall almost at the same time —at t_Z = 3.17 for the 1-P case and at t_Z = 3.2 for the 2-P one. Hence, no important differences are observed due to the deactivation of the air phase.

In Test 3, H is in good agreement with experimental data, though it is noted a lower homogeneity in the fall of the column on the central part of the plot, due to the irregularity of the UNSTR mesh. According to Z , the results are very close to the other experiments, and the little mismatch is due to the difficulty of measuring exactly the same point on different meshes.

Snapshots of the liquid-phase time evolution are shown in Fig. (9) for Test 2. In detail, Figs. (9(a)) and (9(b)) correspond to the initial collapse of the water column, whose front reaches its maximum speed at t_Z 2.3. Then, as shown in Fig. (9(c)), the wave impacts the front wall and, after a transition period, it starts flowing in the opposite direction, Fig. (9(d)). From this point on, there is a lack of clear references in the literature for the description of the flow evolution. However, the wavefront presented here follows its path without further losses of mass, and continues inverting its flow direction each time it encounters a wall, until the initial potential energy is totally dissipated.

Finally, in order to further assess the mesh convergence of the method, a convergence study on progressively finer Cartesian meshes is performed.

The relative Euclidean norm, ε_2, and infinite norm, ε_∞, of the error is evaluated for the H and Z values, in the form

$$\varepsilon_2 = \sqrt{\varepsilon_1^2 + \cdots + \varepsilon_t^2}, \qquad \varepsilon_\infty = \max\left(|\varepsilon_1|, \ldots, |\varepsilon_t|\right), \tag{49}$$

where the relative error ε_t at point x_c is evaluated at each time t as

$$\varepsilon_t = \frac{|\eta(x_c, t) - \eta_{ref}(x_c, t)|}{|\eta_{ref}(x_c, t)|}, \tag{50}$$

with $\eta(x_c, t)$ representing the numerical solution. As no analytical solution is available, the reference values, $\eta_{ref}(x_c, t)$, are taken to be the ones numerically obtained on a very fine mesh with 1.3×10^6 cells ($\Delta h \approx 0.7 \times 10^{-3}$). The results are plotted in Fig. (10), demonstrating a first- to second-order of accuracy as mesh size is decreased. This behavior is consistent with the conclusions extracted in Sec. 4.1.

4.4.1. Time savings

The computational savings resulting from the deactivation of the light phase are quantified in this section. These are obtained comparing the simulation time of the dam break problem on a Cartesian mesh for the 1-P and 2-P approaches, and are expressed in percentage form for three different mesh sizes, Δh. In detail the differences in time step, Δt, number of iterations to solve the Poisson linear system, $ITER$, and the total time-to-solution are given in Tab. 3. Three main observations are extracted from the results.

Δh	Δt	ITER	t_{tot}
5.8×10^{-3}	-32%	-80%	-22%
2.9×10^{-3}	+27%	-78%	-38%
1.45×10^{-3}	+25%	-77%	-47%

Table 3: Differences in % between the 2-P and 1-P approaches regarding time step, Δt, number of iterations to solve the Poisson linear system, $ITER$, and total simulation time, t_{tot}, when varying the mesh size.

The first is that the percentage of reduction in $ITER$ is fairly constant for all cases. The underlying reason is the reduction in ill-posedness of the Poisson linear system as the light phase is deactivated. The second observation is the increase in time step for the fine-mesh cases, which is consequence of the minimization in spurious currents. Last but not least, is that the overall time-to-solution is reduced for all cases, and this difference is larger as the mesh is densified. For instance, a 47% of reduction in time required to solve the dam break problem is obtained for the finest mesh.

4.5. Dam Break 3-D

Once tested on the 2-D dam break problem, the single-phase scheme is further assessed on a 3-D configuration. The problems concerns the evolution of a collapsing water column interacting with a solid box in a 3-D domain. The initial column, depicted in Fig. (11), is contained in a tank of 3.2 m with a square cross section of side 1 m, while the solid box —short sides of 0.16 m and long side of 0.4 m—, is placed at d = 1.17 m from the initial water column front.

The results of the simulations are compared to the experimental data obtained at the *Maritime Research Institute Netherlands* (MARIN) [47], and reported by Kleefsman et al. [24]. These refer to the collapse of a water column with dimensions H = 0.55 m and L = 1.22 m on the described set-up. The available data consists of: (1) the height of the water column at the center of the domain (z = 0.5 m) for x = 0.56 m (H1) and x = 2.22 m (H2); (2) the relative pressure of the water at points P1 $(2.39, 0.025, 0.5)$ m, front of the solid box, and P2 $(2.487, 0.16, 0.5)$ m, top of the box.

The geometry is discretized by means of an unstructured tetrahedral mesh with 1.1×10^6 cells, distributed more densely in the zone where the passage of the interface is expected; see Fig. (12). The domain presents no-slip boundary conditions at the solid walls, while Neumann conditions are imposed at the top boundary. Once more, a pure UP convection scheme is used for the discretization of ϕ_f, while, as in the 2-D case, ϕ_{lim} is set to 0.01.

The evolution in time of the liquid-gas interface is presented in Fig. (13). The initial collapse of the column presents a well-defined linear front, until the point in which the obstacle is reached, resulting in a total rupture of the liquid stream. After colliding with the box, the liquid phase encounters the wall of the domain, producing a bounced wave (1^{ST} WAVE) —depicted in Fig. (13(c))— that starts flowing in the opposite direction. This 1^{ST} WAVE travels back to the left wall, where it slams and inverts again its direction (2^{ND} WAVE), as shown in Fig. (13(d)). Finally, the simulation ends at t = 6 s, approximately when the 2^{ND} WAVE encounters once more the wall at the

right side of the domain.

The numerical results are compared against experimental data in Figs. (14) and (15). First, the water height for H1 and H2 is plotted in Fig. (14), showing its qualitatively good agreement with experiments. In detail, the water height for H1 reduces correctly during the initial water column collapse, rises when the 1ST WAVE reaches the H1 location, and results in a second height peak due to the passage of the 2ND WAVE. This is further corroborated by noticing that the water front reaches H2 at the correct time (around t = 0.33 s), shows a maximum height during the recombination phase (approximately at t = 1.8 s), and shows a second peak corresponding to the passage of the 2ND WAVE (roughly at t = 5.0 s), with a short delay in comparison to the experimental solution. Similarly, as demonstrated in Fig. (15), the pressure evolution for P1 and P2 is well captured by the numerical simulation. The sudden pressure increase shown for P1 at time t = 0.2 s, indicating the instant in which the water front reaches the box, is correctly captured as shown in Fig. (15(a)). Following this peak value, the pressure slowly reduces, and it only increases again during the passage of the 2ND WAVE (around t = 5.0 s). The pressure signal for P2 accurately captures the peak corresponding to the recombination phase that precedes the 1ST WAVE formation (approximately t = 1.68 s).

The numerical results reported in [24] and plotted in Figs. (14) and (15), are obtained on a Cartesian mesh with 1.2×10^6 cells. These also present differences in comparison to the experimental data when the water column

reaches the obstacle zone. This confirms that the small uncertainty between the various results is acceptable when taking into account the complexity and sensibility of the experimental data. Similar conclusions can be extracted from the numerical results recently presented for the same test case by Gu et al. [48].

In summary, the numerical results obtained by means of the single-phase scheme presented in this work are in good agreement with the experimental data. This fact further demonstrates the potential of the method to accurately solve free-surface flows on complex 3-D geometries discretized with fully unstructured meshes.

5. Conclusions

The potential of a new single-phase scheme to accurately reproduce the physics of free-surface flows based on the conservative level-set method has been assessed. The utilization of the level-set function for the identification of the interface allows a straightforward deactivation of the light phase, and leads to the unnecessity to extend the velocity field for its correct advection.

The method has been demonstrated to work properly on both hexahedral and tetrahedral meshes, since different validation tests are correctly reproduced for both grid types. The hexahedral grid —usually distributed according to a hyperbolic law in the free-surface proximity—, is particularly suitable for the simulation of wave motion. On the other hand, the possibility of using unstructured meshes extends the applicability of the method

to very diverse 3-D geometrical configurations. In addition, it allows independent grid densification in particular regions of the domain, for instance, where the passage of the interface or the appearance of turbulence structures is expected.

The adoption of the single-phase solver, instead of a two-phase one, simplifies the resolution of the problem, leading to important advantages in terms of computational time savings. This is due mainly to an increase in time step, as well as a reduction in the number of iterations required to iteratively solve the Poisson's pressure linear system. Moreover, the numerical stability of the simulations is increased due to an overall reduction of the density difference at interfaces.

The scheme has proven to satisfactorily work for the simulation of marine applications. In particular, its capability to reproduce the behavior of solitary and progressive waves, makes it suitable for the numerical simulation of ocean waves interacting with fixed or anchored structures. Possible applications are the analysis of water impact loadings on marine structures, or performance evaluation of offshore devices for energy extraction.

Aknowledgments

This work has been financially supported by the Ministerio de Economía y Competitividad, Secretaría de Estado de Investigacíon, Desarrollo e Innovacíon, Spain (ENE-2014-60577-R and ENE-2011-28699), a FI Grant by AGAUR (Generalitat de Catalunya), a PDJ 2014 Grant by AGAUR (Gen-

eralitat de Catalunya) and by Termo Fluids S.L.

References

[1] Scardovelli R., Zaleski S. (1999). Direct numerical simulation of free-surface and interfacial flow. Annual Review of Fluid Mechanics, 31, 567–603.

[2] Hu H.H., Patankar N.A., Zhu M.Y. (2001). Direct Numerical Simulations of Fluid-Solid Systems Using the Arbitrary Lagrangian-Eulerian Technique. Journal of Computational Physics, 169, 427–462.

[3] Unverdi S.O., Tryggvason G. (1992). A front-tracking method for viscous, incompressible, multi-fluid flows. Journal of Computational Physics, 100, 25–37.

[4] Gorokhovski M., Herrmann M. (2008). Modeling primary atomization. Annual Review of Fluid Mechanics, 40, 343–366.

[5] Hirt C.W., Nichols B.D. (1981). Volume of fluid (VOF) method for the dynamics of free boundaries. Journal of computational physics, 39, 201–225.

[6] Youngs D.L. (1982). Time-dependent multi-material flow with large fluid distortion. Numerical methods for fluid dynamics, 24, 273–285.

[7] Wang Z., Yang J., Stern F. (2012). A new volume-of-fluid method with

a constructed distance function on general structured grids. Journal of Computational Physics, 231, 3703–3722.

[8] Ivey C.B., Moin P. (2012). Conservative volume of fluid advection method on unstructured grids in three dimensions. Center for Turbulence Research Annual Research Briefs, 179–192.

[9] Jofre L., Lehmkuhl O., Castro J., Oliva A. (2014). A 3-D Volume-of-Fluid advection method based on cell-vertex velocities for unstructured meshes. Computers & Fluids, 94, 14–29.

[10] Jofre L., Borrell R., Lehmkuhl O., Oliva A. (2015). Parallel load balancing strategy for volume-of-fluid methods on 3-D unstructured meshes. Journal of Computational Physics, 282, 269–288.

[11] Ito K., Kunugi T., Ohno S., Kamide H., Ohshima H. (2014). A high-precision calculation method for interface normal and curvature on an unstructured grid. Journal of Computational Physics, 273, 38–53.

[12] Osher S., Sethian J. (1988). Fronts propagating with curvature-dependent speed: Algorithms based on Hamilton-Jacobi formulations. Journal of Computational Physics, 79, 12–49.

[13] Sussman M., Smereka P., Osher S. (1994). A Level Set Approach for Computing Solutions to Incompressible Two-Phase Flow. Journal of Computational Physics, 114, 146–159.

[14] Olsson E., Kreiss G. (2005). A conservative level set method for two phase flow. Journal of Computational Physics, 210, 225–246.

[15] Olsson E., Kreiss G., Zahedi S. (2007). A conservative level set method for two phase flow II. Journal of Computational Physics, 225, 785–807.

[16] Balcázar N., Jofre L., Lehmkuhl O., Castro J., Rigola J. (2014). A finite-volume/level-set method for simulating two-phase flows on unstructured grids. International Journal of Multiphase Flow, 64, 55–72.

[17] Balcázar N., Lehmkuhl O., Jofre L., Rigola J., Oliva, A. (2016). A coupled volume-of-fluid/level-set method for simulation of two-phase flows on unstructured meshes. Computers & Fluids, 124, 12–29.

[18] Yang A., Chen S., Yang L., Yang X. (2014). An upwind finite volume method for incompressible inviscid free surface flows. Computers & Fluids, 101, 170–182.

[19] Zhang Y., Zou Q., Greaves D. (2010). Numerical simulation of free-surface flow using the level-set method with global mass correction. International Journal of Numerical Methods in Fluids, 63, 651–680.

[20] Desjardins O., Moureau V., Pitsch H. (2008). An accurate conservative level set/ghost fluid method for simulating turbulent atomization. Journal of Computational Physics, 227, 8395-8416.

[21] Shukla R. K., Pantano C., Freund J. B. (2010). An interface capturing

method for the simulation of multi-phase compressible flows. Journal of Computational Physics, 229, 7411–7439.

[22] Löhner R., Yang C., Oñate E. (2007). Simulation of flows with violent free surface motion and moving objects using unstructured grids. International Journal of Numerical Methods in Fluids, 53, 1315–1338.

[23] Lv X., Zou Q., Zhao Y., Reeve D. (2010). A novel coupled level set and volume of fluid method for sharp interface capturing on 3D tetrahedral grids. Journal of Computational Physics, 225, 2573–2604.

[24] Kleefsman K.M.T., Fekken G., Veldman A.E.P., Iwanowski B., Buchner B. (2005). A Volume-of-Fluid based simulation method for wave impact problems. Journal of Computational Physics, 206, 363–393.

[25] Carrica P.M., Wilson R.V., Stern F. (2007). An unsteady single-phase level set method for viscous free surface flows. International Journal of Numerical Methods in Fluids, 53, 229–256.

[26] Di Mascio A., Broglia R., Muscari R. (2007). On the application of the single-phase level set method to naval hydrodynamic flows. Computers & Fluids, 36, 868-886.

[27] Enright D., Nguyen D., Gibou F., Fedkiw R. (2003). Using The Particle Level Set Method And A Second Order Accurate Pressure Boundary Condition For Free Surface Flows. Proceedings of 4th ASME-JSME Joint Fluids Engineering Conference.

[28] Balcázar N., Lehmkuhl O., Rigola J., Oliva, A. (2015). A multiple marker level-set method for simulation of deformable fluid particles. International Journal of Multiphase Flow, 74, 125–142.

[29] Balcázar N., Lehmkuhl O., Jofre L., Oliva, A. (2015). Level-set simulations of buoyancy-driven motion of single and multiple bubbles. International Journal of Heat and Fluid Flow, 56, 91–107.

[30] Perot B. (2000). Conservation properties of unstructured staggered mesh schemes. Journal of Computational Physics, 159, 58–89.

[31] Jofre L., Lehmkuhl O., Ventosa J., Trias F.X., Oliva A. (2014). Conservation Properties of Unstructured Finite-Volume Mesh Schemes for the Navier-Stokes Equations. Numerical Heat Transfer, Part B: Fundamentals, 65, 53–79.

[32] Trias F.X., Lehmkuhl O. (2011). A self-adaptive strategy for the time integration of navier-stokes equations. Numerical Heat Transfer, Part B: Fundamentals, 60, 116–134.

[33] Chorin, A.J. (1968). Numerical solution of the Navier-Stokes equations. Mathematics of computation, 22, 745–762.

[34] Shewchuk J.R. (1994). An introduction to the conjugate gradient method without the agonizing pain.

[35] Veldman A.E.P., Lam K.W. (2008). Symmetry-preserving upwind dis-

cretization of convection on non-uniform grids. Applied Numerical Mathematics, 58, 1881–1891.

[36] Trias F.X., Lehmkuhl O., Oliva A., Pérez-Segarra C.D., Verstappen R.W.C.P. (2014). Symmetry-preserving discretization of NavierStokes equations on collocated unstructured grids. Journal of Computational Physics, 258, 246-267.

[37] Verstappen R.W.C.P., Veldman A.E.P. (2003). Symmetry-preserving discretization of turbulent flow. Journal of Computational Physics, 187, 343-368.

[38] Fuster D. (2013). An energy preserving formulation for the simulation of multiphase turbulent flows. Journal of Computational Physics, 235, 114–128.

[39] Sweby P. K. (1984). High resolution schemes using flux limiters for hyperbolic conservation laws. SIAM journal on numerical analysis, 21, 995–1011.

[40] Gottlieb S., Shu C. W. (1998). Total variation diminishing Runge-Kutta schemes. Mathematics of computation of the American Mathematical Society, 67, 73–85.

[41] Kang M., Fedkiw R.P., Liu X.D. (2000). A boundary condition capturing method for multiphase incompressible flow. Journal of Scientific Computing, 15, 323–360.

[42] Schillaci E., Balcázar N., Lehmkuhl O., Jofre L., Castro J. (2014). A free surface model for the numerical simulation of oscillating water column systems. In ECFD VI, European Conference on Computational Fluid Dynamics.

[43] Wu G.X., Taylor R.E., Greaves D.M. (2001). The e□ect of viscosity on the transient free-surface waves in a two-dimensional tank. Journal of Engineering Mathematics, 40, 77–90.

[44] Mei C.C., Stiassnie M., Yue D.K.P. (2005). Theory and Applications of Ocean Surface Waves. World Scientific. 657–658, 681–688.

[45] Martin J.C., Moyce W.J. (1952). Part IV. An experimental study of the collapse of liquid columns on a rigid horizontal plane. Philosophical Transactions of the Royal Society of London. Series A, Mathematical and Physical Sciences, 244(882), 312–324.

[46] Sheu T.W., Yu C.H., Chiu P.H. (2009). Development of a dispersively accurate conservative level set scheme for capturing interface in two-phase flows. Journal of Computational Physics, 228, 661–686.

[47] Maritime Research Institute Netherlands (MARIN), Webpage: www.marin.nl/web/show.

[48] Gu H.B., Causon D.M., Mingham C.G., Qian L. (2013). Development of a free surface flow solver for the simulation of wave/body interactions. European Journal of Mechanics-B/Fluids, 38, 1–17.

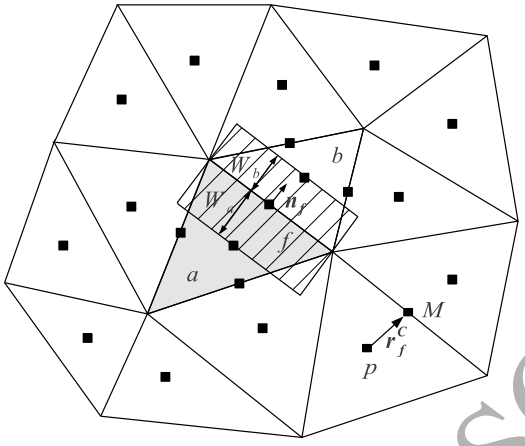

Figure 1: Main geometrical variables involved in the staggered discretization of the equations of fluid motion on a 2-D unstructured mesh. An example of a cell control volume is highlighted in gray, while a face control volume is represented by the dashed area.

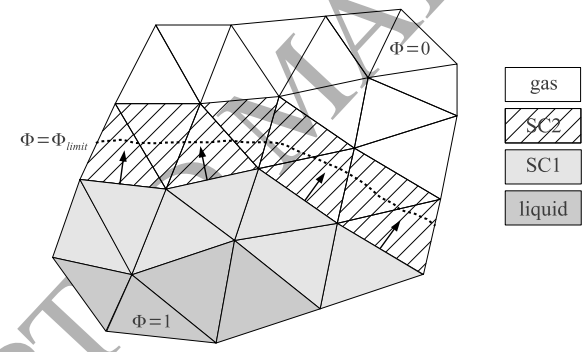

Figure 2: Example of the cells tagging required for the deactivation of the light phase as function of the interface position. The interface is indicated by the fine dashed line.

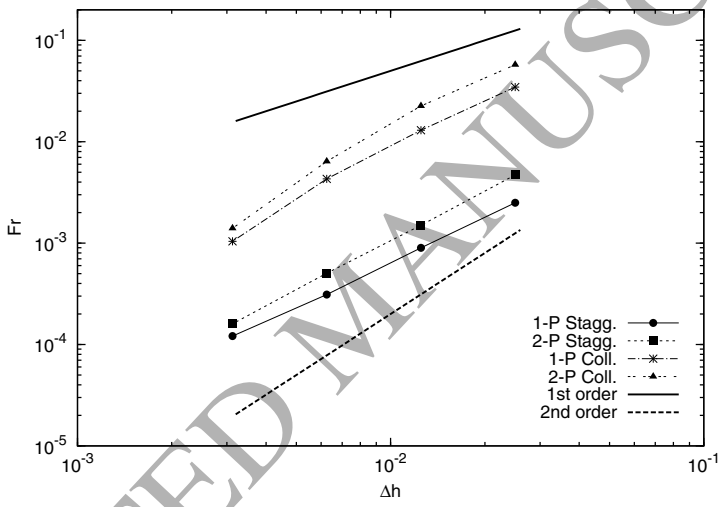

Figure 3: Froude number as function of mesh size for the static liquid column problem. The numerical tests are performed by means of the single-phase (1-P) and full-domain (2-P) models, and according to staggered (Stagg.) and collocated (Coll.) discretizations.

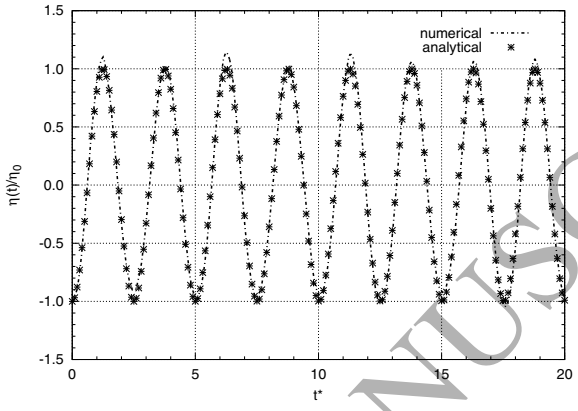

(a) Re 1×10^6

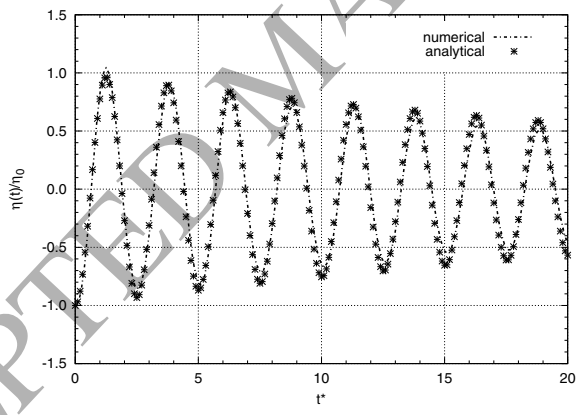

(b) Re 1×10^3

Figure 4: Evolution of the wave height at the center of the domain for the wave sloshing experiment: (a) High Re number, (b) Low Re number. Comparison between analytical values and numerical results obtained on a 2-D Cartesian mesh.

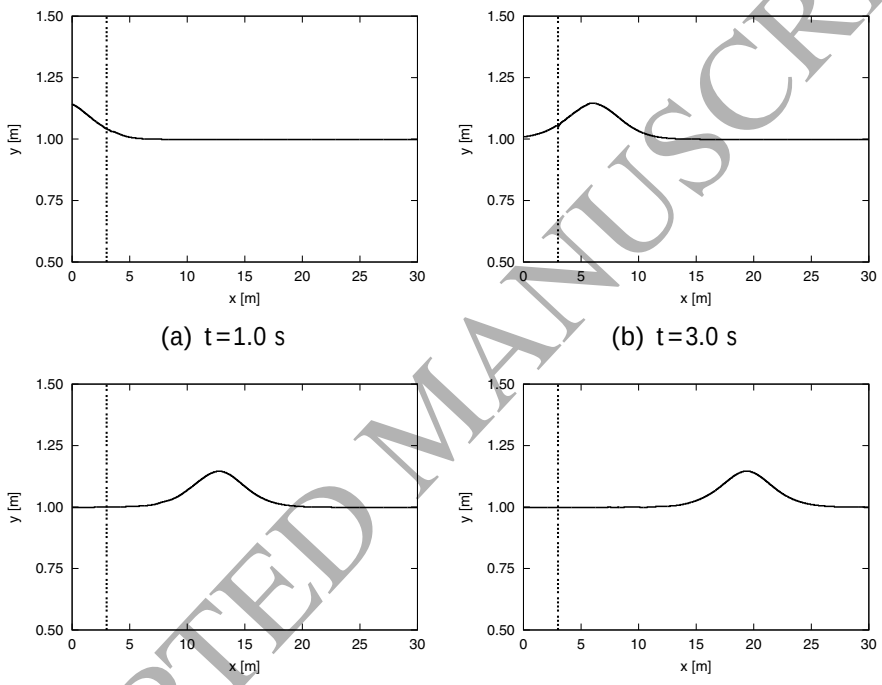

(a) t=1.0 s (b) t=3.0 s

(c) t=5.0 s (d) t=7.0 s

Figure 5: Evolution of the 2-D profile of a solitary wave. The dashed line delimits the wave maker zone.

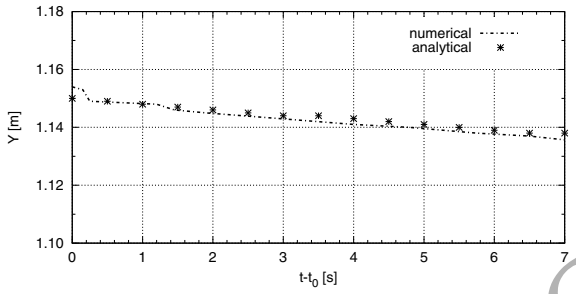

(a)

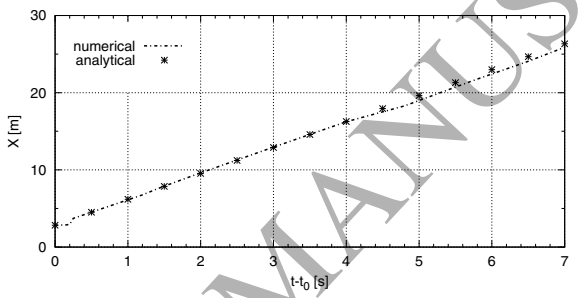

(b)

Figure 6: Evolution of wave height and crest position of a solitary wave along time. Comparison between numerical results and analytical values. t_0 indicates the time at which the wave crest enters the pure numerical zone.

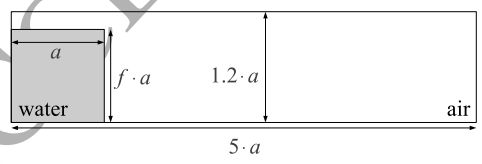

	Water	Air
$\rho\,[\mathrm{kg/m^3}]$	998	1.205
$\mu\,[\mathrm{Pa \cdot s}]$	$1.003 \cdot 10^{-3}$	$1.808 \cdot 10^{-5}$

Figure 7: Initial set-up of the 2-D dam break test and properties of the fluids involved in the simulation.

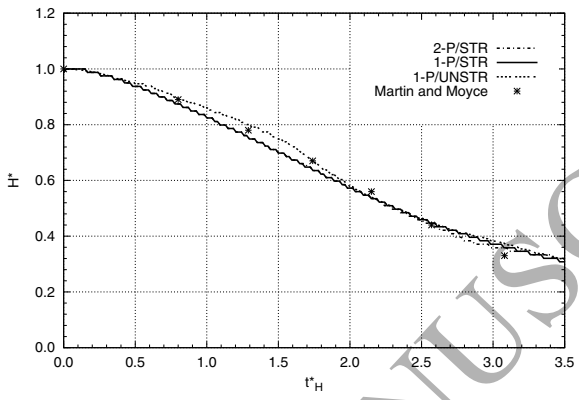

(a)

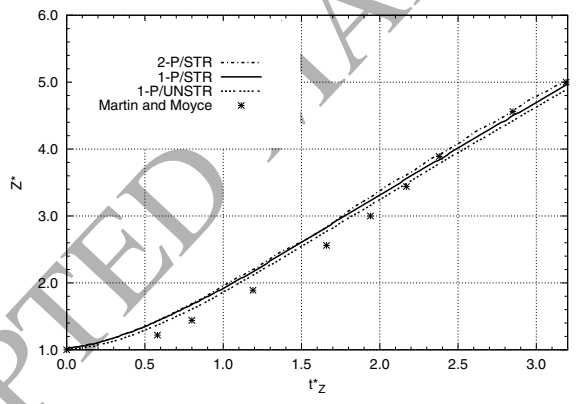

(b)

Figure 8: Evolution of residual water column height, $H^{\square}$, and leading edge, $Z^{\square}$, along time for the 2-D dam break test. Full-domain (2-P) and single-phase (1-P) numerical results, obtained on Cartesian (STR) and unstructured (UNSTR) grids, are compared to experimental reference values [45].

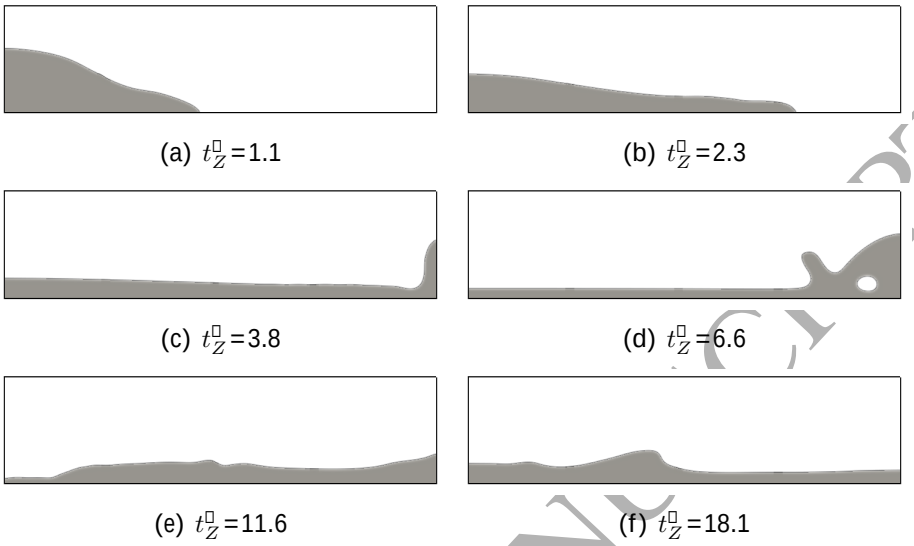

Figure 9: Time evolution of the collapsing 2-D water column simulated by means of the single-phase model (Test 2).

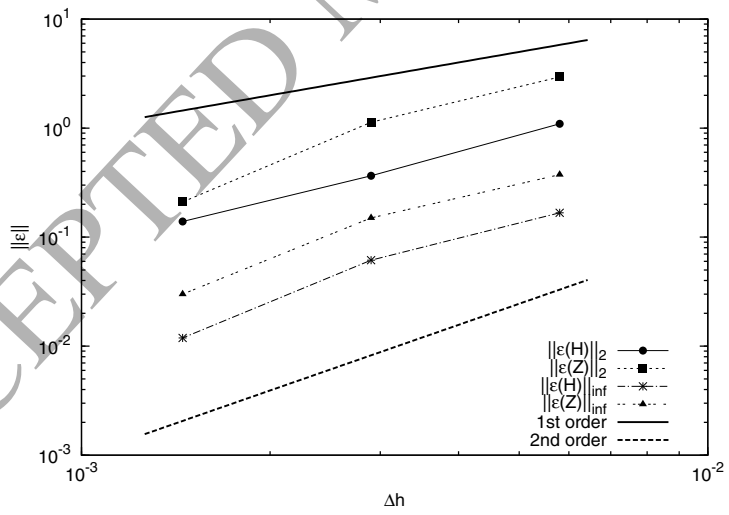

Figure 10: Mesh convergence study performed for the 2-D dam break test. Euclidean norm, ε_2, and infinite norm, ε_{inf}, of the error are reported, referring both to Z and H.

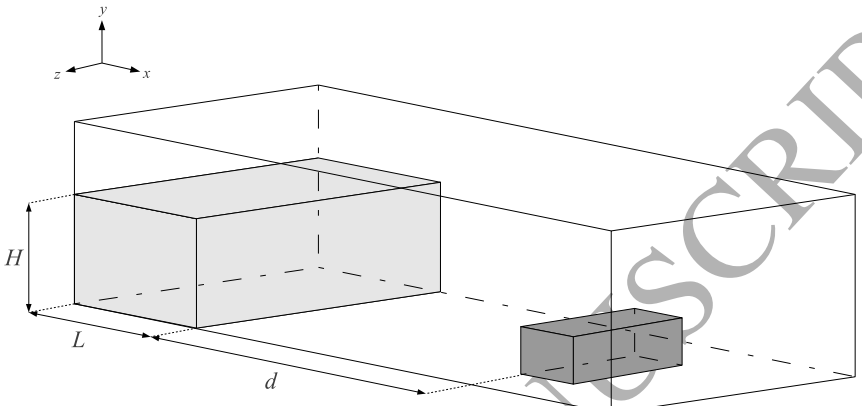

Figure 11: Initial set-up of the 3-D dam break simulation.

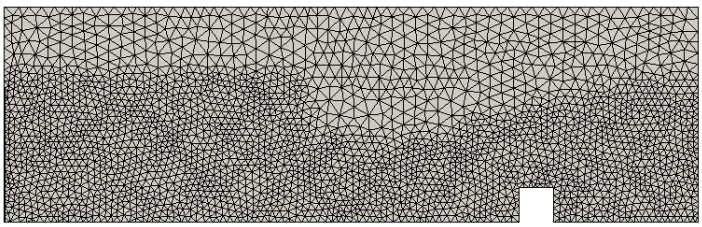

Figure 12: Slice of the tetrahedral mesh used for the simulation of the 3-D dam break. The mesh density is increased at the regions in which the passage of the flow is expected.

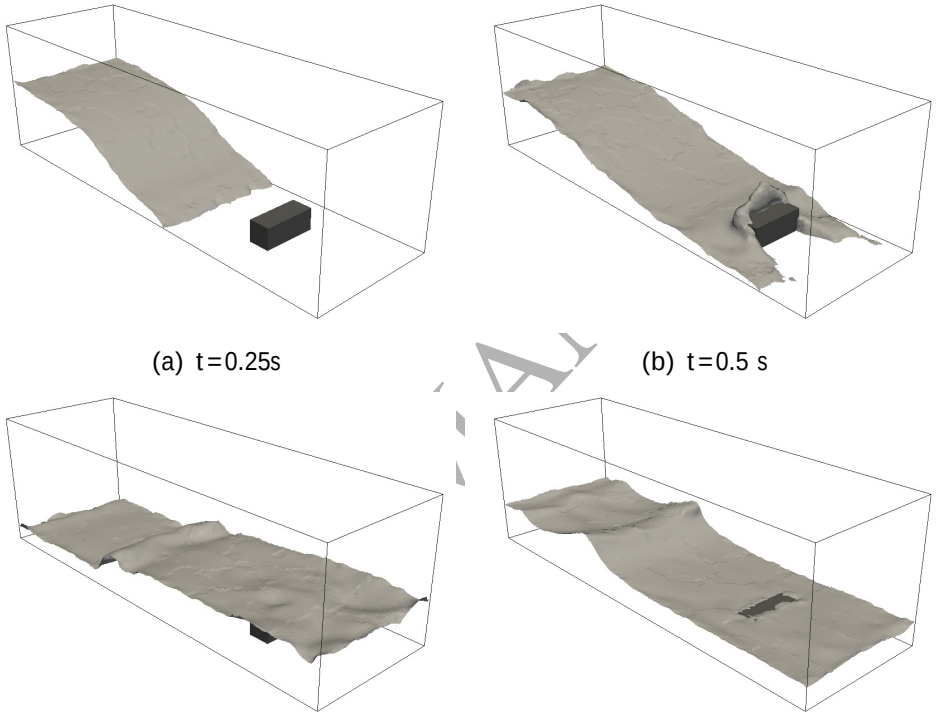

(a) t=0.25s (b) t=0.5 s

(c) t=2.58 s (d) t=4.54 s

Figure 13: Instantaneous snapshots of the flow evolution for the 3-D dam break simulation. The represented surfaces correspond to the contour plots of $\phi(\mathbf{x}, t)$ = 0.5.

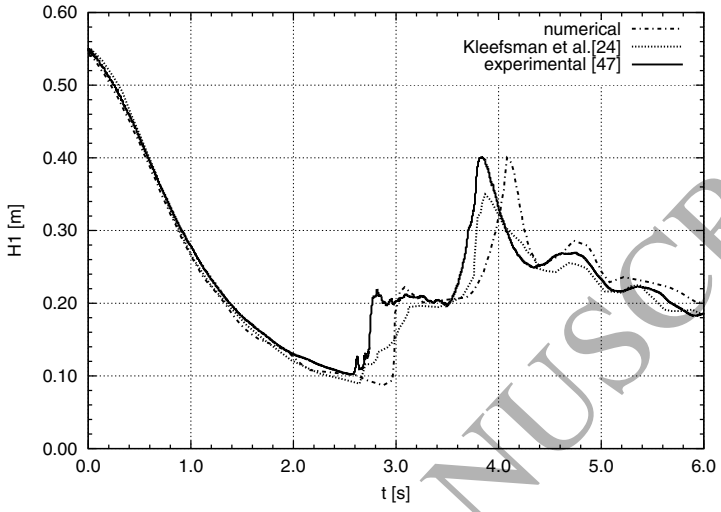

(a)

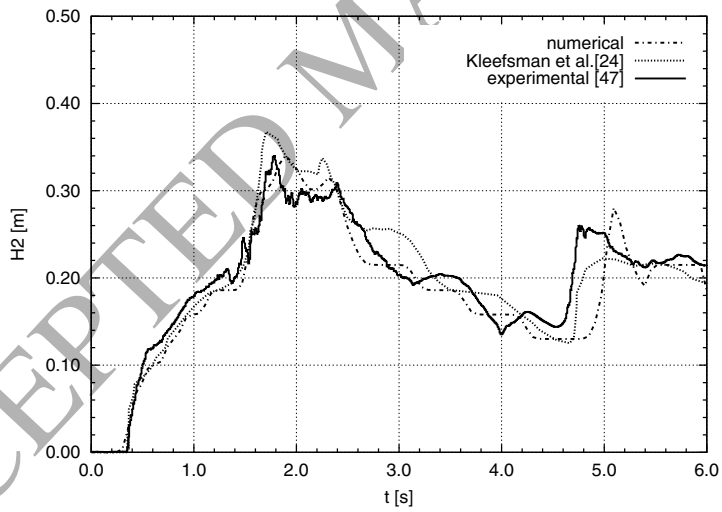

(b)

Figure 14: Water column height measured at points H1 and H2 for the 3-D dam break numerical simulation and references [24, 47].

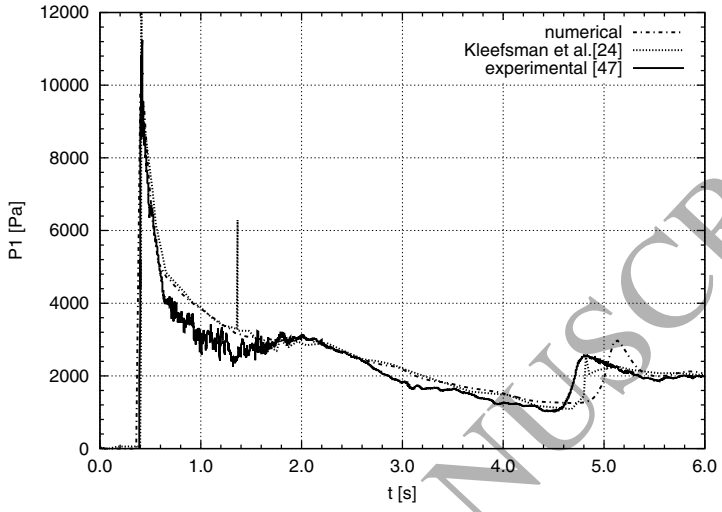

(a)

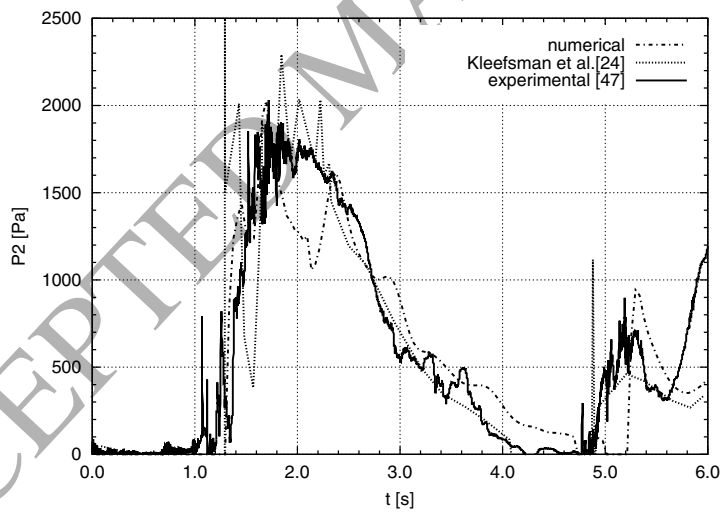

(b)

Figure 15: Pressure measured at probe points P1 and P2 for the 3-D dam break numerical simulation and references [24, 47].